# Dynamically Evolving Metastability in an Atomic Hourglass: Temporal Control of the Metal-Insulator Transition of $VO_2$ by a Mobile Dopant

Diane G. Sellers, <sup>1,2</sup> Erick J. Braham, <sup>1,2</sup> Ruben Villarreal, <sup>3</sup> Baiyu Zhang, <sup>2</sup> Abhishek Parija, <sup>1,2</sup> Timothy D. Brown, <sup>2</sup> Theodore E.G. Alivio, <sup>1,2</sup> Heidi Clarke, <sup>2</sup> Luis R. De Jesus, <sup>1,2</sup> Lucia Zuin, <sup>5</sup> Xiaofeng Qian, \*<sup>2</sup> Raymundo Arroyave, <sup>2,3,4</sup>\* Patrick J. Shamberger, <sup>2</sup>\* Sarbajit Banerjee <sup>1,2</sup>\*

E-mail: <u>feng@tamu.edu</u>; <u>raymundo.arroyave@tamu.edu</u>; <u>patrick.shamberger@tamu.edu</u>; <u>banerjee@chem.tamu.edu</u>

# **Abstract:**

Transformations between different atomic configurations of a material oftentimes bring about dramatic changes in functional properties as a result of the simultaneous alteration of both atomistic and electronic structure. Transformation barriers between different polytypes are generally changed through compositional modification, which however alters relative phase stabilities in an immutable manner. Continuous modification of transformation temperatures post hoc to synthesis remains much more challenging but holds potential for endowing distinctive memory of thermal history with promise for applications in neuromorphic computing, chronometry, thermometry, and sensing. Using the canonical metal—insulator transition in VO<sub>2</sub> as an example, we demonstrate that mobile dopants that are weakly coupled to the lattice provide a means of imbuing an entirely reversible and dynamical modulation of the phase transformation of VO<sub>2</sub>. Specifically, we demonstrate the remarkable time-dependent evolution of the relative phase stabilities of insulating monoclinic (M<sub>1</sub>) and metallic rutile (R) phases of VO<sub>2</sub> in an "hourglass" fashion as interstitial boron species relax from high-energy sites wherein they are situated upon a thermally induced phase transition. The relaxation process corresponds to a 50°C range of the transition temperature achieved within the same sample as a function of residence time and temperature. The diffusive boron dopant atoms provide a means of attaining a reconfigurable and readable time- and thermal history dependent response that derives from intrinsic material properties.

<sup>&</sup>lt;sup>1</sup>Department of Chemistry, Texas A&M University, College Station, TX 77843, USA

<sup>&</sup>lt;sup>2</sup>Department of Materials Science and Engineering, Texas A&M University, College Station, TX 77843, USA

<sup>&</sup>lt;sup>3</sup>Department of Mechanical Engineering, Texas A&M University, College Station, TX 77843, USA <sup>4</sup>Department of Industrial and Systems Engineering, Texas A&M University, College Station, TX 77843, USA

<sup>&</sup>lt;sup>5</sup>Canadian Light Source, University of Saskatchewan, Saskatoon, Canada

## **Introduction:**

The presence of adjacent minima within free energy landscapes of periodic solids (along axes such as temperature, pressure, strain, or alloying) allows for reversible switching of properties as a result of the structural rearrangement of atoms. A structural transformation along such landscapes oftentimes brings about pronounced alterations of electronic structure and accompanying electronic, ferroelectric, optical, and magnetic properties; such modulations of functional properties have been utilized for diverse applications spanning the range from neuromorphic computing to thermochromic windows, 1-3 memory storage, 4 and transformation toughening. 5,6 Martensitic transitions, which are characterized by the reversible and diffusionless motion of atoms upon a spontaneous change in symmetry of the unit cell are particularly facile and provide numerous examples wherein the hysteresis between forward and reverse transitions can be controlled through compositional modulation and strain.<sup>7,8</sup> Compositional modulation through doping or alloying generally changes the relative phase stabilities of adjacent wells and the barrier to the transformation between the wells in an immutable manner, enabling the trapping of metastable phases under ambient conditions. Much less studied is the role of dopants that are diffusive in nature, are weakly coupled to the lattice, and whose mobility thereby endows a dynamical aspect to the relative phase stabilities of the adjacent wells. In this article, we utilize a canonical metal—insulator transition material VO<sub>2</sub> to demonstrate a remarkable time-dependent evolution of the relative phase stabilities of insulating monoclinic (M<sub>1</sub>) and metallic rutile (R) phases (in an "hourglass" fashion) as a diffusive dopant species relaxes from a high-energy site wherein it is initially positioned upon a thermally induced phase transition. Such an in situ modulation of phase stabilities creates a detectable thermal-history-dependent signal with the heating transition temperature serving as a characteristic readout; remarkably, this signature is completely reset upon returning to the low temperature phase. We determine that the dynamically varying local structure of diffusive B dopant atoms provides a means of accessing this reconfigurable time- and thermal history dependent response that derives from intrinsic material properties.

The ability to realize a history-dependent non-linear response is a key tenet for the creation of neuromorphic architectures, which have attracted considerable interest as a means of energy efficient computing.<sup>1,9</sup> Materials exhibiting pronounced metal—insulator transitions (MIT) underpinned by electron correlation can serve as active elements exhibiting such neuromorphic function provided their temporal response can be rendered programmable. VO<sub>2</sub> is characterized by a change of almost five orders of magnitude in its electronic transport properties upon the MIT at ca. 67°C. The extent of coupling of the electronic Mott transition with a structural M<sub>1</sub>—R transition has been the subject of much controversy.<sup>10–13</sup> The introduction of dopant atoms alters the phase stabilities of insulating M<sub>1</sub> and metallic R phases and the heights of the barriers between them. In the case of tungsten as a substitutional dopant on the vanadium sublattice, the larger ionic radius of the dopant induces strongly anisotropic strain whereas its hexavalent character results in considerably increased metallicity resulting in an overall destabilization of the low-temperature

M<sub>1</sub> phase with respect to the high-temperature metallic phase. <sup>10,14,15</sup> Other dopants induce the stabilization of altogether different polymorphs; for instance, Cr- and Al-doping (or coherent epitaxial strain) stabilizes the M<sub>2</sub> phase, <sup>16–18</sup> interstitial hydrogen doping stabilizes orthorhombic variants, <sup>19</sup> and Ir doping stabilizes a 1D tunnel-structured phase. <sup>20</sup> The introduction of B atoms as interstitial dopants within VO<sub>2</sub> selectively stabilizes the R phase over the M<sub>1</sub> phase.<sup>21,22</sup> The distinctive location of boron dopants within interstitial sites causes the incorporated boron atoms to be weakly coupled to the anion and cation sublattice imbuing a mobility that results in a dynamical response in the monoclinic phase hitherto not observed for conventional static substitutional dopants. Such a mobility of the interstitially incorporated dopant atoms is shown to be coupled to the stability of the monoclinic phase and modulates the MIT in a novel, resettable, history dependent manner. In this manuscript, we detail the behavior of thermal memory effects in B-doped VO<sub>2</sub> and explore the inherent metastability of B dopants that brings about a kinetically controlled modulation of the MIT temperature across a 45°C temperature range. Analysis of the B local coordination environment as well as the evaluation, via first principles calculations, of B dopant site energies, charge, and diffusion pathways allows for the development of a mechanistic picture of the observed dynamical response.

## **Results and Discussion**

# The Temporally Evolving Metal—Insulator Transition of B-Incorporated VO<sub>2</sub>

VO<sub>2</sub> exhibits a hysteretic martensitic-type first-order transition from a monoclinic M<sub>1</sub> phase to a high-symmetry rutile (R) phase at 67°C. The transition temperature has been shown to be modified through alloying with various dopants to span the range from 23 to 96°C for the heating transition and -19 to 90°C for the cooling transition.<sup>9,22–24</sup> Options for post-synthetically modulating the transition temperature are limited and include the irreversible creation of defects through high-energy irradiation or subjecting nanobeams to tensile strain both of which have limited reversibility.<sup>25,26</sup> The dynamical and reversible modulation of the transition temperature of VO<sub>2</sub> has not thus far been achievable using a chemical vector.

Hydrothermally prepared VO<sub>2</sub> nanoparticles have been reacted with a molecular boroncontaining precursor through rapid thermal annealing to obtain boron atoms lodged in interstitial sites<sup>22</sup> as described in the Methods section and schematically illustrated in **Figure 1A**. **Figure 1B** depicts differential scanning calorimetry (DSC) plots measured for undoped VO<sub>2</sub>, 1.8 at.% Bincorporated VO<sub>2</sub>, and 5.2 at.% B-incorporated VO<sub>2</sub> denoting the critical temperatures ( $T_c$ ) of the heating and cooling transitions based on the maxima of endothermic and exothermic heat flows accompanying the phase transitions, respectively. Incorporation of B atoms depresses the transition temperature by ca. 10°C/at.% B.<sup>22</sup> **Figure 1C** shows powder X-Ray diffraction (XRD) patterns for the same samples acquired at 22°C; the full diffraction patterns and scanning electron microscopy images of the samples are shown in **Figure S1**. The (001) reflection of the monoclinic phase shifts slightly to lower 2 $\theta$  values upon doping with 1.8 at.% B; Rietveld refinement of the diffraction patterns of B-incorporated VO<sub>2</sub> and VO<sub>2</sub> nanoparticles subjected to rapid thermal annealing without the molecular precursor (**Tables S1 and S2, Figures S2 and S3**) demonstrate B incorporation brings about a slight lattice expansion along the a and c axes resulting in a 0.4% increase in volume. No evidence is observed for crystalline boron oxides or orthorhombic/M<sub>2</sub> phases of VO<sub>2</sub>, which have been reported previously to be associated with interstitial hydrogen incorporation,<sup>27</sup> substitutional doping of trivalent cations,<sup>28</sup> and anisotropic strain.<sup>29</sup>

Indeed, evidence for interstitial instead of substitutional incorporation is derived from (i) B K-edge XANES spectra that will be discussed below, which has been assigned with the help of XCH-XAS calculations delineating spectral fingerprints for trigonal and tetrahedral interstitial sites; (ii) high-angle annular dark-field scanning transmission electron microscopy images indicating no modulation of intensity on vanadium sites and concomitant electron energy loss spectra showing the presence of boron atoms within the VO<sub>2</sub> lattice;<sup>22</sup> (iii) the ability to eliminate B atoms from the lattice by annealing to a temperature of 500°C, wherein no substitutional dopant can be thus removed; and (iv) extensive density functional theory calculations that will be presented below contrasting the stability of boron incorporation at interstitial and substitutional sites.

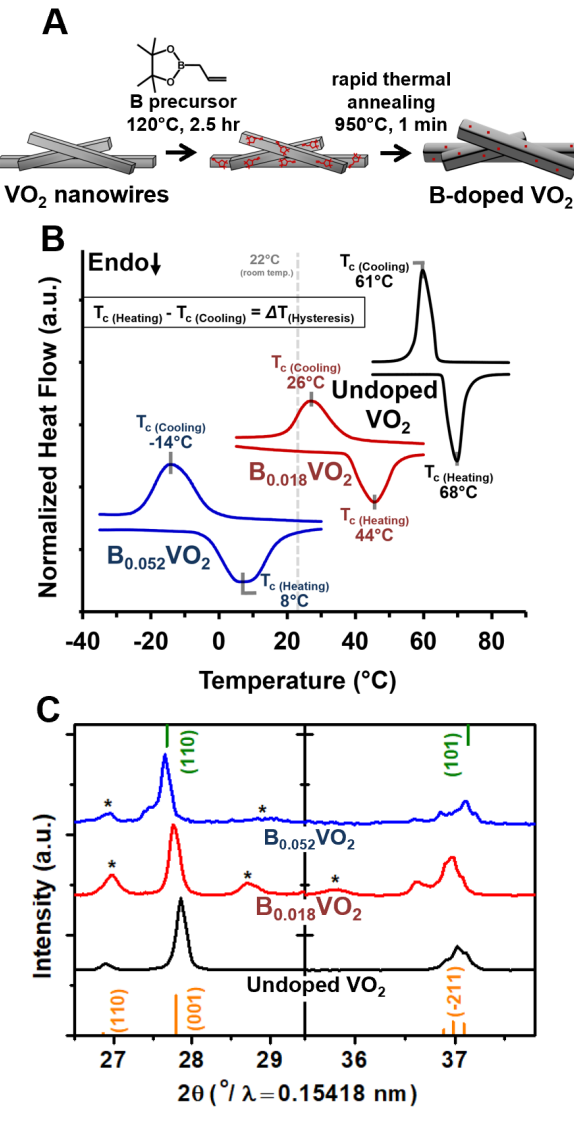


Figure 1: Synthesis and Characterization of B-incorporated VO<sub>2</sub> nanoparticles

A) Schematic illustration of the diffusive doping of B atoms in VO<sub>2</sub> nanobeams. B) DSC traces measured for  $B_{0.052}VO_2$ ,  $B_{0.018}VO_2$ , and undoped VO<sub>2</sub> acquired at a scan rate of 10°C/min and offset along the vertical axis for clarity. The critical transition temperatures ( $T_c$ ) are designated as the peaks of the exothermic and endothermic heat flows for the heating and cooling scans, respectively. A monotonic depression of the phase transition is observed as a function of the B concentration. Additionally, the width of hysteresis  $\Delta T_{(Hysteresis)}$  between the heating and cooling transitions is increased from 7°C for undoped VO<sub>2</sub> to 18 and 22°C for  $B_{0.018}VO_2$  and  $B_{0.052}VO_2$ , respectively. C) Powder XRD patterns for  $B_{0.052}VO_2$ ,  $B_{0.018}VO_2$ , and undoped VO<sub>2</sub> in the 2 $\theta$  range from 26—29.5° and 35.2—38.2°. Reflections corresponding to the  $M_1$  phase of VO<sub>2</sub> are plotted along the bottom horizontal axis as per Joint Committee on Powder Diffraction Standards (JCPDS) #. 043-1051, whereas reflections corresponding to the R phase of VO<sub>2</sub> are plotted along the top horizontal as per JCPDS# 79-1655. Undoped and  $B_{0.018}VO_2$  samples are indexed to the  $M_1$  phase of VO<sub>2</sub>, whereas the pattern for the  $B_{0.052}VO_2$  sample is indexed to the R polymorph of VO<sub>2</sub>. The

incorporation of B atoms depresses the  $M_1 \to R$  transition temperature by ca. 10°C/at.%  $B^{22}$  such that the observed stabilization of R polymorph at room temperature for the  $B_{0.052}VO_2$  sample is consistent with a depression of the critical transition temperature for 5.2 at.% B-doping. Reflections derived from a minority  $V_8O_{15}$  phase (JCPDS no. 71-0041) are asterisked<sup>22</sup> but do not contribute to the observed MIT behavior.<sup>30</sup>

Figure 2 exhibits the results of differential scanning calorimetry (DSC) experiments performed on VO<sub>2</sub> nanoparticles incorporating 5.2 at.% boron that illustrate the dynamical behavior of this material. Figure 2A shows the overlaid thermal profiles of 49 experimental heat treatment cycles performed on the same sample systematically varying isothermal hold time (intervals of 15, 30, 45, 60, 90, 120, and 180 min) and the isothermal temperature (from -50 to 10°C). Figure 2B plots the resulting  $T_c$ , the temperature corresponding to peak heat flow for the heating transition,<sup>31</sup> as a function of isothermal hold time and temperature. The measured transition temperatures reflect unique coordinates specific to the thermal and chronological history of the samples, which derive from the dynamical diffusion of B atoms in the M<sub>1</sub> phase as will be elucidated below. Figures 2C and D show DSC data corresponding to slices of the 2D array in Figure 2A illustrating the effects of increasing isothermal temperature (held at a constant 90 min isothermal time) and isothermal time (held at a constant -10°C isothermal temperature), respectively. All temperature changes throughout this series of experiments, cooling from the R phase to -60°C, heating to the isothermal hold temperature, and heating from the isothermal hold temperature back to the R phase, were performed at a rate of 10°C/min. Intriguingly, the corresponding cooling  $R \to M_1$  transition was observed to show no analogous dynamical shift of the transition temperature (Figure S4). Figure S4 further shows that B incorporation distinctively alters the rate-dependence of the heating transition as compared to undoped VO<sub>2</sub>; the transition is shifted to a higher temperature at slower rates, corresponding to increased residence time in the M<sub>1</sub> phase.

Figure 2B illustrates a pronounced increase in the heating transition temperature as a function of both isothermal residence time and temperature. At the lowest isothermal temperature of -50°C, a residence time of 180 min does not substantially alter the transition temperature as compared to not having an isothermal period. In contrast, holding the sample at 10°C for an interval of 180 min shifts the transition temperature upwards by greater than 15°C. A window between -30°C up to the transition temperature is observed wherein the time spent alters the transition temperature of the heating  $M_1 \rightarrow R$  transition, and is hereafter denoted as the "annealing" regime. Within this regime, the elapsed time is directly correlated with an increase of the  $M_1 \rightarrow R$  transition temperature; the latter experimental observable provides a precise "clock"-like measure of the time elapsed after cooling. In other words, the results suggest that a thermally activated process is operational below the  $M_1 \rightarrow R$  transition temperature, which governs the state of the system from which the subsequent  $M_1 \rightarrow R$  phase transition is launched. The quenched system appears to remain in a higher energy state (and can be transitioned back to the R phase at a lower

temperature), whereas the relaxed or annealed system appears to be at lower energy and correspondingly transitions to the R phase at a higher temperature.

The grey surface in Figure 2B denotes an Arrhenius kinetic fit indicating a thermally activated process. A single population model was built using a single activation energy ( $E_a$ ) of 0.96 eV assuming a  $1e10^{13}$  attempt frequency (A) and proved a poor fit for the experimental data (**Figure S5A**). A series of five activation energies centered around 0.98 eV (in increments of  $\pm 0.04$  eV) was examined to model a continuum of activated processes contributing to the observed dynamic relaxation of this material (**Figure S5B**). This model assumes fractions of B-doped VO<sub>2</sub> in the sample such that the total observed relaxation is a summation of their effects with  $\phi_i$  representing the fraction of the whole population with a given  $E_a$  such that the sum of i fractions equals 1. Assuming five equal fractions such that  $\phi_i = 1/5$  of  $E_a^i = [0.90, 0.94, 0.98, 1.02, 1.04]$  and an attempt frequency (A) of  $1e10^{13}$  the relaxation of each fraction from metastable  $[B]_{ms}$  to relaxed  $[B]_{rel}$  is calculated as a first order rate:

$$[B]_{ms}^{i} = \phi_{i}[B]_{ms} \dots (1)$$

$$\frac{\partial [B]_{rel}^{i}}{\partial t} = \frac{-\partial [B]_{ms}^{i}}{\partial t} = k^{i}[B]_{ms}^{i} \dots (2)$$

$$k^{i} = Ae^{\left(\frac{-Ea^{i}}{kT}\right)} \dots (3)$$

Such a model provides a substantially improved fit to the observed phenomenology and is the function plotted as the grey surface in **Figure 2B**. The improved fit is thought to arise from variations in dopant concentrations, inhomogeneous strain, or defects, across ensembles of particles, which alter diffusion pathways of boron atoms, altering the barrier height of this activated process around the central barrier of 0.98 eV as discussed in greater detail below. A phenomenological sketch of the dynamic activated process is summarized in **Figure 2E** and illustrates the remarkable resettability of the process. In every case, regardless of the thermal profile adopted to probe the sample and irrespective of the extent of relaxation, the effect is reset when transitioning back from the R phase.

Additional experimentation contrasted the effects of heating and cooling rates on the transitions of two differently doped samples (**Figure S4**) with that of undoped VO<sub>2</sub>. Also, the effects of varying transition rates independently and the effects of additional cooling in the  $M_1$  phase (**Figure S6**) were examined. **Figure S4** shows a smaller rate dependence of the cooling transition for the B-incorporated samples as compared to undoped VO<sub>2</sub> suggesting easier nucleation of the  $M_1$  phase in the doped samples, which is ascribed to the presence of more potent nucleation sites. <sup>10,32</sup> The heating transition shifts to higher temperature with slower rates which is concordant with the conclusion from **Figure 2** that the thermal history in the  $M_1$  phase allows for modulation of the  $M_1$  to R transition temperature as a function of time and temperature. The extent

of cooling was found to have negligible effect. In summary, the data show (1) that applying sufficient thermal energy to the system while maintaining in the  $M_1$  phase relaxes the system from a quenched to a relaxed state, and (2) that the extent of transformation between the unrelaxed (quenched) and relaxed states follows an Arrhenius exponential dependence on the annealing temperature. Both observations denote the operation of a thermally activated process for B-doped  $VO_2$  in the  $M_1$  phase that does not have parallels in undoped  $VO_2$ .

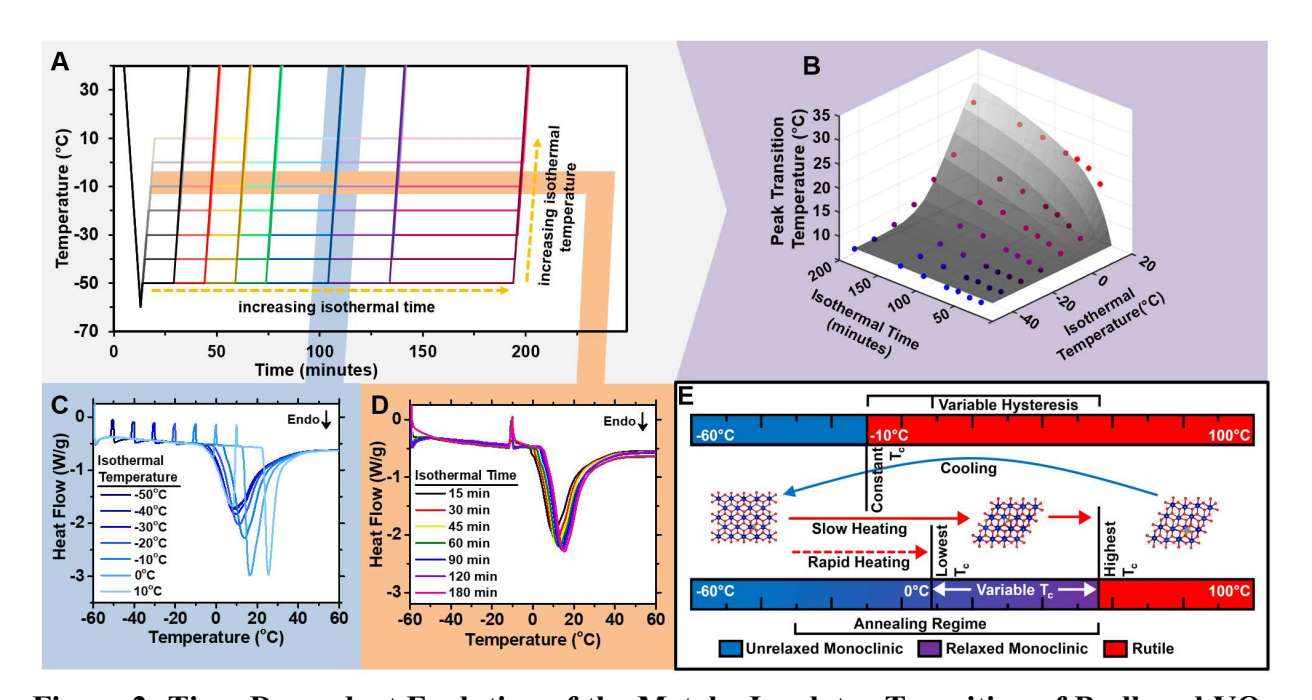


Figure 2: Time-Dependent Evolution of the Metal—Insulator Transition of B-alloyed VO<sub>2</sub>. A) Thermal profiles of DSC experiments probing structural relaxation kinetics within the  $M_1$  phase of  $B_{0.052}VO_2$ . The series of measurements shown in panels C and D are highlighted with blue and orange bars, respectively. B) A three-dimensional representation of  $T_c$  as a function of isothermal

annealing temperature and time for the thermal profiles shown in (A), an Arrhenius model is overlaid for comparison (see also Figure S5). C) DSC traces corresponding to a series of measurements scanned at 10°C/min from -60 to 100°C with 90 min isothermal annealing intervals at temperatures ranging from -50 to 10°C. D) DSC traces of a series of measurements scanned at 10°C/min from -60°C to 100°C with isothermal annealing at -10°C for time intervals ranging from 15 to 180 min. For A-D the cycles where the material was held at 0°C and 10°C contain a population of particles that have transitioned to the R phase before annealing. The observed shift is recorded for the fraction that had remained M<sub>1</sub> as seen in panel C as the lightest blue/furthest shifted peak. E) Schematic illustrating the time-dependent variation of transformation temperature of VO<sub>2</sub> as derived from the DSC measurements.

The *in-situ* DSC annealing experiments plotted in Figure 2 provide insight into the dynamics of the relaxation process on relatively short timescales. In an attempt to explore the maximal limit of the relaxed state, a more gradual thermal ramp spanning the course of 7 days has been performed

using a programmable water bath. The utilization of a slow ramp rate allows for the annealing temperature to slowly increase as the  $M_1 \to R$  transition increases (due to the relaxation process) allowing for the highest annealing temperature possible. The temperature has been increased following the sequence plotted in Figure 3A for two samples to access intermediate and fully relaxed states. The upper portion of Figure 3A displays the first cycle of the DSC trace following removal from the water bath. The black curve represents the second cycle where the B<sub>0.052</sub>VO<sub>2</sub> sample once again reflects the 8.5°C T<sub>c</sub> of the quenched state indicating that the sample has been reset after transitioning from  $M_1 \rightarrow R$ . The DSC trace of the first relaxation experiment (labeled "intermediate") has been subjected to a stepwise decrease in ramp rate, shown in blue, and exhibits two endothermic features, one sharp feature at 39.3°C and another smaller and broader transition at 56.3°C, representing two different populations within the sample. The DSC trace of a second water-bath-aided relaxation experiment (labeled "relaxed") has been subjected to a still slower exponential decrease in ramp rate, shown in red, and exhibits a primary endothermic transition at 53.2°C and a smaller shoulder at 55.8°C. All subsequent water bath/DSC relaxation experiments for this sample exhibit transitions at ca. 56°C (or lower) indicating that this value corresponds to a quasi-equilibrium limit for this B-doped VO<sub>2</sub> sample. Figure 3A illustrates that the magnitude of the  $T_c$  shift spans a remarkable 45°C from a quenched sample (transitioning at 8.5°C) to a fully relaxed state (transitioning at 53.2°C). The  $M_1 \rightarrow R$  transformation peak is further greatly sharpened upon relaxation suggestive of a convergence or funneling of the population distributions within this sample to a quasi-equilibrium state. Figure S7A shows analogous data for  $B_{0.018}VO_2$ , which has been simply allowed to relax at room temperature for 40 and 323 days, evolving from a  $T_c$  of 44.1°C for the quenched sample to an intermediate state of 53.5°C after 40 days, and a  $T_c$ of 58.1°C corresponding to the fully relaxed state after 323 days. Notably, the relaxation process does not correspond to the expulsion of B from the lattice since the observed behavior is completely reversible upon further thermal cycling as demonstrated in **Figure S7B**, which shows the following cycle directly after transitioning from a relaxed state mirrors the scan taken before relaxation occurred.

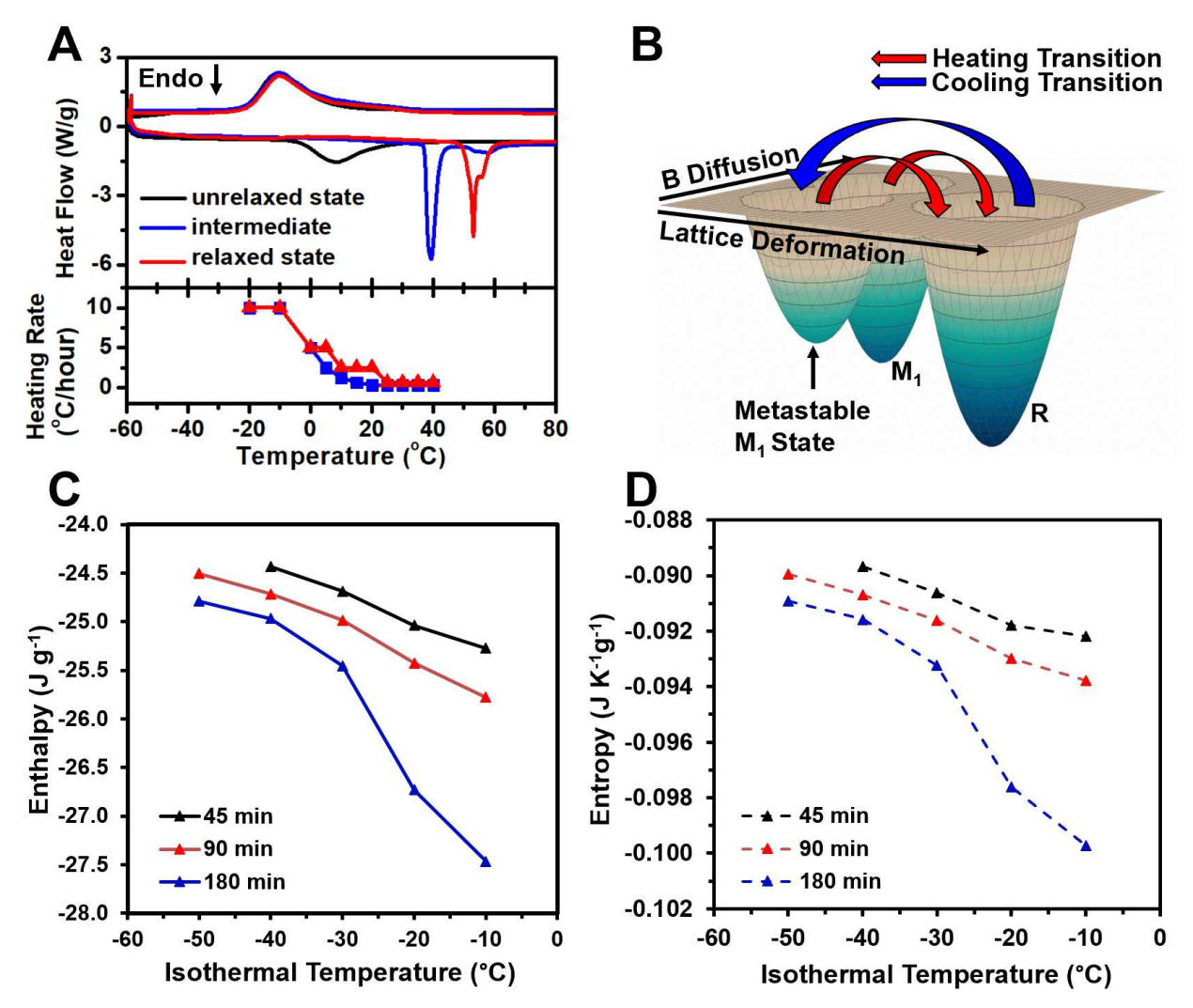


Figure 3: Evidencing a Thermally Activated Process below the Phase Transition. A) DSC traces of  $B_{0.052}VO_2$  immediately upon cooling (quenched or "unrelaxed" state) and for the same sample upon relaxation from -20°C—40°C within an external water bath at different temperature ramp rates (corresponding rates are shown in the lower plot) amounting to intermediate and fully relaxed structures. B) Illustration of energy landscape of the MIT transition as a function of temperature of the system and diffusion of B atoms between interstitial sites. C, D) evolution of  $\Delta H$  and  $\Delta S$  respectively as a function of isothermal temperature for isothermal times of 45, 90, and 180 min, as outlined in Figure 2A for the  $B_{0.052}VO_2$  sample.

In terms of energy landscapes of structural transformations, the data (**Figure S7B**) suggest that following the  $R \to M_1$  phase transition (akin to resetting of the "hourglass"), the  $M_1$  lattice is positioned in a higher-energy metastable state that is only slightly lower in energy as compared to the R state and can thereby be readily transitioned back to the latter state at low temperatures. However, given sufficient time and thermal energy, the metastable state can relax through a thermally activated process to the lowest-energy quasi-equilibrium state of the  $M_1$  phase, which is

substantially lower in energy as compared to the metastable state and thereby transitions at a higher temperature (**Figure 3B**). According to this hypothesis, the phase transformation temperature is indicative of the extent of relaxation from the quenched metastable to the relaxed quasi-equilibrium structure (akin to time-variant flow within the hourglass) and as such, reflects the thermal history and elapsed time since the last "reset".

In order to further examine the thermodynamics of the phase transformation and better understand the dynamical modulation of the transition temperature upon boron incorporation, we have evaluated the latent heat (M) of the M1  $\rightarrow$  R transition with respect to enthalpic (H) and entropic (S) contributions. Latent heat (M) has been calculated by integration of the exothermic DSC trace for a series of isothermal annealing experiments from the combinations of isothermal time and temperature variations depicted in Figure 2A. During a first-order phase transition, the free energy (G = H-TS) for the M1 phase is equal to that of the R phase giving  $\Delta H = T_c \Delta S$  when  $G = \Delta H$ . Using this relationship, when  $G = \Delta H$ , the latent heat can be plotted and evaluated for  $\Delta H$  and  $\Delta S$  contributions. **Figure 3C and D** shows  $\Delta H$  (A) and  $\Delta S$  (B) as a function of isothermal temperature for annealing times of 45, 90, and 180 min. A correlated change in both entropy and enthalpy is observed when the metastable quenched state is annealed to the relaxed state. The correlation of entropy and enthalpy shows that the change in the thermodynamic stability of the M1 and R phases as illustrated in Figure 3 B is driven by both a change in the relative phase enthalpy and electronic entropy (the doping changes not lattice enthalpy but also conduction entropy differential). This behavior is consistently observed across all of the samples.

The presence of multiple transformation peaks in the intermediate relaxed state (Figure 3A) suggests a hierarchy of metastable states within the landscape. The broad range of transition temperatures in the quenched sample (Figure 3A) suggests that immediately following the  $R \rightarrow$ M<sub>1</sub> transition, the VO<sub>2</sub> lattice relaxes into an array of shallow-energy metastable states such that a relatively broad distribution of thermal energies can bring about a transformation back to the R phase (but there is only a relatively small differential separating the metastable M<sub>1</sub> states and the R state). Annealing at temperatures below the T<sub>c</sub> allows the lattice to overcome the activation energy barrier associated with transitioning to quasi-equilibrium states; multiple metastable states relax into a narrow distribution of quasi-equilibrium states, thereby narrowing the observed endotherm for the  $M_1 \rightarrow R$  transition from such states (Figure 3A). Nucleation to the R phase from these lower-energy relaxed states requires overcoming a greater energy differential, which is manifested in higher transition temperatures. Beyond the "hourglass" idea of relaxation into the quasi-equilibrium state, an important finding from the perspective of functional applications is the ability to tune the heating transition (and therefore hysteresis) for the same exact sample across a range of 45°C adjacent to room temperature simply based on thermal history without any alteration of composition.

## **Unraveling the Atomistic Origins of the Hourglass**

We now turn our attention to delineating the atomistic origins of this dynamically evolving low-temperature transformation, which constitutes the second axis in Figure 3B. Since such a

phenomenon has not been observed in undoped or other previously reported strained or substitutionally doped VO<sub>2</sub> systems,  $^{10,13,14,20}$  it is reasonable to infer that the B dopant plays a distinctive role in the dynamics of the  $M_1 \rightarrow R$  transition. It is worth noting that unlike the vast majority of dopants examined for VO<sub>2</sub>, B is able to diffuse across the VO<sub>2</sub> lattice owing to its small atomic radius (0.88Å for four-coordinate B atoms)<sup>33</sup> and high diffusivity.<sup>21,22</sup> One possible origin of differences between the quenched and relaxed state is a change in the strain profile across the system as a result of B diffusion.<sup>10,14</sup> However, powder XRD measurements acquired at -163°C for relaxed and quenched states of the  $B_{0.052}\text{VO}_2$  sample are shown in **Figure S8** and are superimposable with no discernible shifts that would indicate a transition dominated by alleviation of strain effects (thermal relaxation profiles used are shown in **Figure S9**).

Given the absence of significant changes in the average structure of the VO<sub>2</sub> lattice and in light of the relatively long relaxation timescales between metastable and quenched states, the specific sites occupied by B atoms warrant further attention and have been evaluated with the help of density functional theory (DFT) calculations at the generalized gradient approximation (GGA)+Hubbard U theory level. While DFT is limited in its treatment of electron correlated materials, the large supercells required to model the low dopant concentrations render the materials here intractable by dynamical mean field theory approaches.  $^{11,34,35}$  We have converged on a U parameter (U = 3.4 eV) that captures the electronic structure of the two polymorphs (**Figure S10**). The use of a large unit cell and a U parameter that accounts for electron correlation enables us to use the DFT calculations to guide spectral interpretation and to develop a physically intuitive albeit inevitably reductionist (in the absence of accurate determination of energetics) model of the phenomena under consideration.

Within their respective unit cells, six  $M_1$  and three R unique interstitial sites have been identified by applying symmetry operations (defined by the respective space groups) on the 68 geometrically determined sites located using the AFLOW software package.<sup>36</sup> The formation energies ( $E_f$ ) of each unique interstitial site has been calculated using DFT such that  $E_f$  is defined as:

$$E_{\rm f} = E(BVO_2) - E(VO_2) - E(B) \dots (4)$$

where  $E(BVO_2)$  is the total energy of a VO<sub>2</sub> supercell containing one B atom (BV<sub>32</sub>O<sub>64</sub>, corresponding to 3.1 at.% B incorporation in VO<sub>2</sub>),  $E(VO_2)$  is the energy of an undoped VO<sub>2</sub> supercell, and E(B) is the energy of a single B atom based on a 36 atom unit cell (space group:  $R\overline{3}m$ ). This supercell size is in the range of experimentally observed B concentrations while still being computationally tractable in DFT+U calculations. Coordinates and  $E_f$  values for each interstitial location within the M<sub>1</sub> and R unit cell are listed in **Tables S3** and **S4**, respectively. Upon transition from a rutile state, the doped supercell adopts a metastable distortion around the boron atom that does not occur when substituting boron into a monoclinic M<sub>1</sub> lattice as a starting point. To simulate the generation of possible metastable states caused by the boron defect across the R  $\rightarrow$  M<sub>1</sub> phase transition, a rutile-like configuration was used as a starting point for the relaxation. This structure was generated by shifting the vanadium atoms of a monoclinic supercell by linear interpolation towards the R structure, which increases uniform spacing along the c-axis and

reduces twisting of the vanadium pairs. From this starting configuration, the ions were relaxed back to a monoclinic configuration resulting in the metastable  $M_1$  configuration. This metastable state has a different lowest energy configuration for the boron position than is found in the relaxed monoclinic  $M_1$  phase or the R phase. **Figures 4A-C** depict the lowest energy interstitial sites for B atoms in the R phase, metastable  $M_1$  phase, and relaxed  $M_1$  phase, respectively. **Figure 4D** shows normalized  $E_f$  values for the interstitial locations of B sites in the R and metastable  $M_1$ , and  $M_1$  supercells where  $M_1(1)$  and  $M_1(1)^*$  as well as  $M_1(5)$  and  $M_1(5)^*$  are the symmetrically equivalent sites with the asterisk denoting the metastable  $M_1$  distortion. All stable sites have a tetrahedral coordination with neighboring oxygen atoms, except the trigonally-coordinated  $M_1(6)^*$ , which is the lowest energy boron position of the distorted metastable  $M_1$  state shown in Figure 4C. The three lowest energy sites highlighted in red in Figure 4D are posited to correspond to the path traversed by boron atoms from the transition from rutile to unrelaxed monoclinic to relaxed monoclinic. Notably, a small thermal population of boron atoms may occupy higher energy sites, but given the relative energetics the most stable sites are expected to be strongly favored.

To better understand the nature of the interstitial boron atoms, the formation energies have been evaluated for different charged states of boron and contrasted to the stability of substitutional defects on the cation and anion sublattice. Calculation methodologies are detailed in the Methods section. Figure 4E and F show the defect diagrams of boron associated interstitial and substitutional defects under O-rich and O-poor conditions, respectively. To determine the equilibrium Fermi level at the synthesis temperature, we calculated the formation energy of native defects, as shown in Figure S13. The equilibrium Fermi level under O-rich and O-poor condition is pinned around 0.5 eV and 0.55 eV at the synthesis temperature. In both condition, the most stable defect is boron interstitial defect (B<sub>i</sub>) with 3+ state. Moreover, a substitutional boron on the vanadium site (B<sub>V</sub>) may be occupied as a minority defect type. The density of states for the monoclinic and rutile phases are shown in Figure S10, confirming that the calculations capture the insulating nature of the monoclinic phase and the metallic nature of the rutile phase. We also notice that (+2/0) and (0/-2) transition level of B<sub>V</sub> is located around 0.5 eV above the VBM with unstable +1 and -1 charge states, indicating that By exhibits a negative U behavior. Such behavior is also found in B<sub>0</sub>. Additional analysis of the top valence states and the orbital resolved density of states, as detailed in the supporting information, suggest that no deep defect states are localized on the boron atom and thus no strong lattice relaxation around B is observed. Our results indicate that it is likely due to the screened Hartree-Fock like exchange effect in the Hubbard U correction that was applied to the DFT calculations.

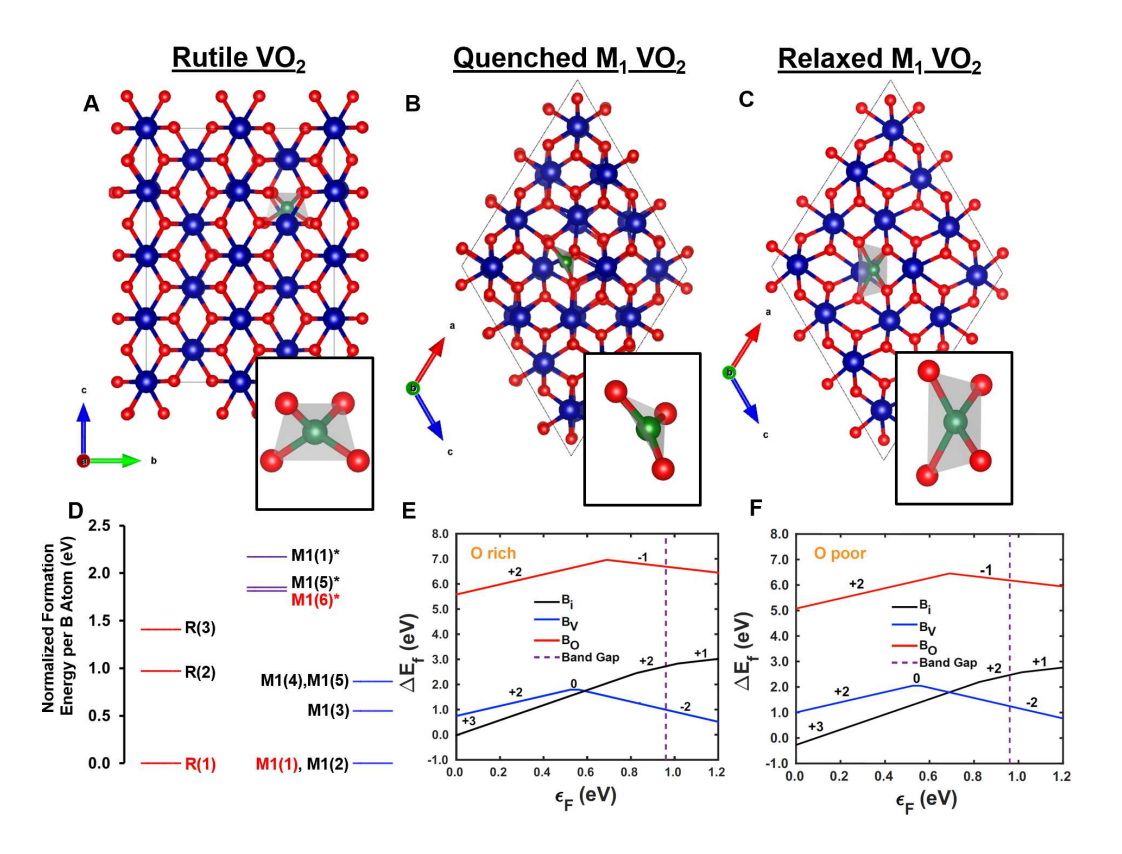


Figure 4. Energetics of Boron Interstitial Sites in VO<sub>2</sub> and Delineation of Spectroscopic Signatures. A—C) DFT calculated supercell for B-doped VO<sub>2</sub>, illustrating the most thermodynamically favorable interstitial sites for B incorporation for R (A, R(1)), quenched M<sub>1</sub> (B, M1(6)), and relaxed M<sub>1</sub> (C, M1(1)). The oxygen coordination of the boron atoms within these sites are shown as insets. Vanadium atoms are depicted as blue spheres, oxygen atoms as red spheres, and B atoms as green spheres. Lattice parameters for the doped M<sub>1</sub> structure with different concentrations of boron can be found in **Table S5**. D) Normalized formation energies of B incorporation into different interstitial location within the R (red), metastable M<sub>1</sub> (violet), and relaxed M<sub>1</sub> (blue) supercells. **Tables S3** and **S4** catalogue the specific sites and their energetics. E and F display the formation energies of charged defects for oxygen rich and oxygen poor condition, respectively. The energies were calculated for substitutional boron defects at the oxygen sites (B<sub>o</sub>), substitutional boron defects at the vanadium sites (B<sub>v</sub>), and interstitial boron defects (B<sub>i</sub>). For both the oxygen rich and oxygen poor environments the most stable defect at the fermi level of  $\epsilon_F$ =0 is a 3+ interstitial boron defect B<sub>i</sub>.

Experimental evidence for alteration of the B local structure during transformation from the quenched to relaxed state is derived from B K-edge X-ray absorption near-edge structure (XANES) spectroscopy measurements. XANES involves the excitation of core-level electrons to partially occupied and/or unoccupied states and thus serves as a sensitive element-specific probe of electronic structure. Figure 5B plots B K-edge XANES spectra, corresponding to excitation of B 1s electrons to B 2p hybrid states, acquired at room temperature for quenched M1 B<sub>0.004</sub>VO<sub>2</sub>

(red line), relaxed M1 B<sub>0.052</sub>VO<sub>2</sub> (black line), and R B<sub>0.052</sub>VO<sub>2</sub> (blue line). The low B concentration of the B<sub>0.004</sub>VO<sub>2</sub> sample is imperative to obtain a quenched sample that is still in the M<sub>1</sub> phase, since the  $R \to M_1$  transition for  $B_{0.052}VO_2$  is below room temperature (Figure 1B). Spectral signatures in B K-edge XANES spectra can be assigned to specific bonding modes and local coordination environments (a) based on comparison to data acquired for known periodic solids with varying coordination and local symmetry of B sites and (b) first-principles excited state core hole X-ray absorption spectroscopy (XCH-XAS) calculations.<sup>22,38–44</sup> A list of B standards and the corresponding spectral signatures, assignments, and references used in this study are compiled in **Table S6.** Trigonally-coordinated B bonded to oxygen atoms are characterized by absorption features at 194 and 203 eV, corresponding to 1s  $\rightarrow \pi^*$  and 1s  $\rightarrow \sigma^*$  transitions, respectively, to sp²-hybrid B—O final states. Tetrahedrally-coordinated B is defined by an absorption feature at 198 eV, which corresponds to a 1s  $\rightarrow \sigma^*$  transition populating sp<sup>3</sup>-hybrid B—O final states. Also associated with tetrahedrally coordinated B is a feature at 200 eV, which is thought to be a multiple-scattering resonance.<sup>39</sup> When the sample is in the R phase state, the XANES spectrum shows features associated with both trigonal and tetrahedral B-O coordination geometries. However, the spectra measured for relaxed M1 and quenched M1 samples show significant differences. Absorption features in the B K-edge spectrum acquired for relaxed M1 B<sub>0.052</sub>VO<sub>2</sub> are primarily associated with tetrahedral coordination (197—200 eV), with only a small absorption at 194 eV associated with trigonal coordination. In contrast, for the quenched M1 B<sub>0.004</sub>VO<sub>2</sub> sample the opposite is true; absorption features characteristic of tetrahedral coordination are absent and the predominant feature observed is the 1s  $\rightarrow \pi^*$  transition at 194 eV associated with trigonal coordination. The stark change in local electronic structure and coordination between the quenched and relaxed M1 samples indicates a change is coordination geometry from trigonal to tetrahedral geometry during the relaxation, consistent with the most stable B interstitial geometries in metastable M<sub>1</sub> and relaxed M<sub>1</sub> polymorphs inferred from the DFT+U calculations in Figure 4.

The change in local boron coordination environment is more directly corroborated by modeling the B K-edge XANES spectra using DFT for different B interstitial sites. **Figure 5C** shows the B K-edge spectrum calculated using the XAS-XCH<sup>43</sup> approach. The lowest energy tetrahedral sites in the R and M<sub>1</sub> phases as well as an analogous metastable trigonal site to represent the quenched M<sub>1</sub> phase have been calculated. This method provides an orbital-specific description of the origin of the XANES features. The simulated spectra show good agreement with the experimental spectra (with the exception of rutile polymorph, wherein multiple coordination geometries are found to co-exist in the experimental spectrum). Observed transitions in the simulated XANES spectra correspond to the final states depicted in the isosurfaces of Figure 5D-F. Chemically meaningful assignments of the spectral features can be obtained by visualizing these isosurfaces and analyzing their orbital character. The absorption features between 197—200 eV for relaxed M<sub>1</sub> and R structures are assigned to the excitation of a core B 1s electron to a σ\* state corresponding to hybridization between B 2p and O 2p states. An analogous transition for the quenched M<sub>1</sub> structure with trigonal coordination of B atoms is observed between 200—205 eV. The absorption feature for the quenched M<sub>1</sub> at 193.9 eV is assigned to the excitation of a core B

Is electron to a B 2p—O 2p hybrid  $\pi^*$  state. The B 1s  $\to \pi^*$  transition is observed for approximately trigonal planar geometries and is a distinctive spectral signature of interstitial sites occupied by B atoms in quenched  $M_1$  phase. The isosurface assignments are in excellent agreement with the assignments based on B standards (Table S6). Taken together the experimental XANES spectra and XCH-XAS simulations provide definitive experimental evidence for the diffusion of B atoms from trigonal planar to tetrahedral local coordination environments and establish a distinctive spectral signature of B atoms trapped in a metastable site.

The nudged elastic band (NEB) method has been used to examine potential diffusion pathways and energy barriers for B atoms within M<sub>1</sub> VO<sub>2</sub>. 45,46 The initial and final interstitial B sites have been selected as the lowest energy boron position in the metastable quenched state upon transformation from  $R \rightarrow M_1$  transitioning to the lowest energy B site in the undistorted relaxed  $M_1$ state. The XANES spectra of the quenched VO<sub>2</sub> sample suggests an initially trigonal B coordination environment immediately following the  $R \rightarrow M_1$  transition. Our initial starting point is the trigonal M1(6)\* as the most stable state in the quenched distorted M<sub>1</sub> state and whilst the final state is selected as tetrahedral M1(1), the lowest-energy equilibrium site; these selections are fully consistent with the experimental XANES data and its assignments (Figure 5C-F. Whilst many possible diffusion pathways exist for B atoms positioned in some of the higher energy sites shown in Figure 4D, we have plotted the pathway of the M1(6)\* state to the M1(1) state in Figure 5A as the most likely illustrative pathway connecting the lowest lattice energy configurations. The energy barrier for diffusion between the sites is 1.05 eV, which is consistent with barriers deduced from the Arrhenius kinetic modeling of the experimental data shown in Figure 2B and Figure S5. The cooling transition from  $R \to M_1$  may bring B atoms into several metastable states with the M1(6)\* and M1(5)\* close in energy, contributing to the broadness of the  $M_1 \rightarrow R$  transition from the incipient quenched state. The  $M_1 \rightarrow R$  transformation from B situated within the most energetically preferred site requires considerably greater energy given its relative stability with respect to the initial metastable quenched state (as also sketched in Figure 3B). Figure 5A illustrates the change in local coordination of the boron atom upon relaxation from the trigonal M1(6)\* site to the tetrahedral M1(1) site as labeled. The diffusion of B atoms on the timescales observed in this experiment can be attributed to a coupled distortion of the lattice that takes the system out of its metastable quenched state and into its thermodynamic minimum. In summary the B atom finds itself in a metastable state upon transition from  $R \to M_1$  structural transition and relaxes towards the most stable configuration through a thermally activated process.

To the best of our knowledge, there are few parallels to the observed dynamic modulation of the phase transition stemming from intrinsic lattice degrees of freedom (and not just domain switching derived from microstructural properties). There are some parallels to the phenomenon of martensite aging observed in shape memory alloys such as Au–Cu–Zn (L21–M18R)<sup>47</sup> and In–Tl (FCC–FCT; disordered),<sup>48,49</sup> wherein a degree of intrinsic modulation of the symmetry raising transition temperatures and critical stress is observed as a function of kinetic relaxation of the martensitic state. Such phenomena have been attributed to defect migration and the evolution of symmetry conforming defect states.<sup>50</sup>

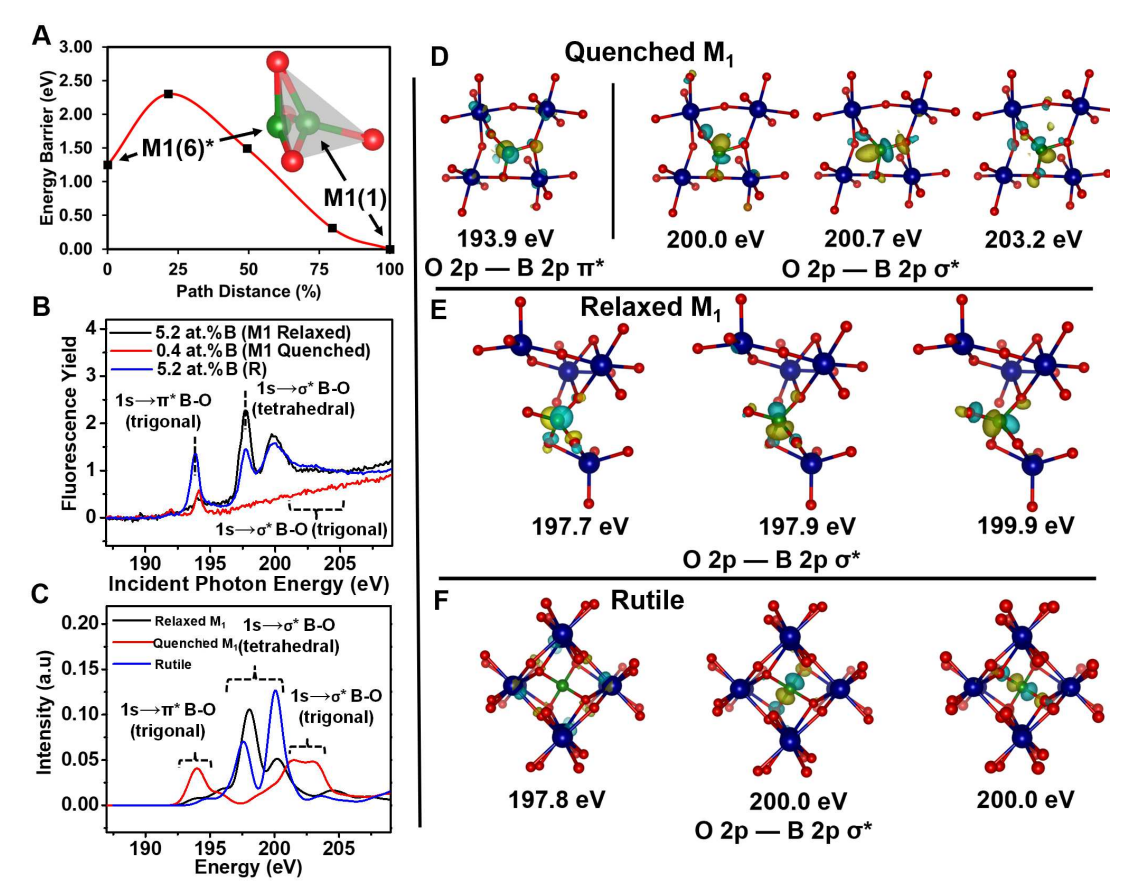


**Figure 5. Boron Diffusion Pathways and Energetics of Diffusion.** A) Energy profile of the minimum energy pathway between the metastable trigonal M1(6)\* site and the lowest-energy tetrahedral interstitial site M1(1) as calculated using NEB. Red spheres represent oxygen atoms; green spheres represent B atoms. B) B K-edge XANES spectra of B-doped VO<sub>2</sub> samples measured at room temperature. The relaxed M<sub>1</sub> B<sub>0.052</sub>VO<sub>2</sub> sample was relaxed *in situ* as described in **Figure S11** and the corresponding DSC scan is shown in **Figure S12**. The quenched-M<sub>1</sub> B<sub>0.004</sub>VO<sub>2</sub> and R B<sub>0.052</sub>VO<sub>2</sub> samples were heated to 100°C and rapidly quenched to 0°C and brought to room temperature immediately prior to the measurement. C) Calculated B K-edge XANES spectra of B-doped VO<sub>2</sub>. Calculated spectra correspond to a low energy relaxed tetrahedral site and an analogous metastable trigonal site. Final state assignments of the spectral features are assigned based on the symmetries of the states observed in the isosurface plots shown in D-F. Features are labeled with their character as assigned from isosurface plots of the final states. Isosurfaces are furthermore labeled with the energy of the transition feature."

#### **Conclusions**

In summary, we demonstrate that incorporation of a mobile interstitial dopant species imbues a means of dynamically modulating the insulator—metal transition temperature of VO<sub>2</sub>. The critical transition temperature of a singular sample can be varied across a temperature range of 45°C (in close proximity of room temperature) based simply on the thermal history and time

elapsed since the material was cooled from the R to the  $M_1$  phase without engineering any change in composition. The dynamic modulation of the transition temperature is explicable considering that the most energetically favored sites for B atoms vary throughout the transition between the M<sub>1</sub> and R polymorphs with an intermediate metastable trigonal state. Consequently, raising the system to the R phase and then cooling it down to the M<sub>1</sub> phase stations the B atom in an energetically disfavored trigonal site and leaves the system in a metastable initial state that is energetically only slightly more stable than the R phase (and can be transitioned to the latter at a lower temperature). Over a period of time, the B atoms are able to diffuse in real space to energetically more favorable tetrahedral configurations through a thermally activated process bringing the system to a quasi-equilibrium arrangement that represents a deeper valley in the free energy landscape. Transformation to the R phase is more hindered from this configuration resulting in a pronounced increase of the transition temperature. Consistent with the idea of an activated atomic diffusion process, the relaxation time exhibits an Arrhenius dependence on temperature. B K-edge XANES along with DFT calculations suggest a short hop from an initially trigonal coordinated site to a tetrahedrally coordinated site as the system relaxes from a quenched metastable structure to the stable monoclinic polymorph. Heating past the  $M_1 \to R$  transition temperature results in the B atoms being situated in higher symmetry sites and serves as a means of resetting the relative populations of metastable and quasi-equilibrium states upon cooling.

The incorporation of B as a mobile dopant thereby endows a temporal history-dependent component to the phase transition that is dependent on the atomistic diffusion barriers encountered by B atoms and that can be readout using the heating transition temperature. In addition to the "hourglass" time and thermal history dependence of the experimentally measured transition temperature, B-doped VO<sub>2</sub> is seen to exhibit a programmable time-variant modulation of conductance, which has potential for utilization in neuromorphic circuits and memory devices. Future work will examine the influence of other diffusive dopant atoms in VO<sub>2</sub> and of B in analogous correlated systems such as NbO<sub>2</sub>.

## **Methods**

Synthesis of VO<sub>2</sub> Nanowires. VO<sub>2</sub> nanowires with lateral dimensions of  $210 \pm 70$  nm and lengths in the range of  $4.0 \pm 3.0$  µm were prepared as reported in our previous work based on the hydrothermal reduction of V<sub>2</sub>O<sub>5</sub> by 2-propanol. Briefly, 1.6000 g of V<sub>2</sub>O<sub>5</sub> (Sigma-Aldrich, St. Louis, MO) was reduced to VO<sub>2</sub> with 10 mL of 2-propanol (Fisher, Fair Lawn, NJ) dissolved in 65 mL of deionized water (prepared with a Barnstead International NANOpure Diamond ultrapure water system  $\rho = 18.2$  M $\Omega$  cm<sup>-1</sup>). The hydrothermal reaction was performed at 210°C for 72 h in a 125 mL autoclave. The supernatant was discarded and the precipitate was rinsed with acetone (Macron Fine Chemicals, Center Valley, PA). The samples were then placed within a quartz tube, which was annealed using a tube furnace to a temperature of 550°C (ramping at a rate of ca. 45°C/min) for 3 h under flowing Ar gas at a rate of 800 mL/min.

**Incorporation of B by Diffusive Doping.** 2-Allyl-4,4,5,5-tetramethyl-1,3,2-dioxaborolane (97%) was purchased from Sigma-Aldrich (St. Louis, MO). In a typical reaction, 20 mg of VO<sub>2</sub> nanowires were dispersed in 1.00 mL of mesitylene by ultrasonication and 200 μL of 2-allyl-4,4,5,5-tetramethyl-1,3,2-dioxaborolane was added to the reaction mixture. The reactants were allowed to stir for 2.5 h at 120°C under an Ar ambient in a Schlenk flask. The VO<sub>2</sub> nanowires were recovered by centrifugation, rinsed with toluene, and annealed using a 2 mL porcelain combustion boat (VWR, Sugar Land, TX) to a temperature of 900—950°C for 1 min under an Ar ambient in a quartz tube furnace as reported in our previous work.<sup>22</sup> Performing the annealing step using VO<sub>2</sub> nanowires without adsorption of the molecular precursor likewise induces sintering of the nanowires; however, in the absence of B atoms, the relative phase stabilities of the monoclinic and rutile phases are essentially unchanged.

**Differential Scanning Calorimetry.** Differential scanning calorimetry (DSC) analysis was performed using a TA instruments Q2000 instrument. Aluminum T-Zero pans were used for DSC experiments under a purge flow of Ar gas. Scan rates were varied from 1°C/min to 15°C/min.

**Powder X-ray Diffraction.** Powder X-ray diffraction (XRD) patterns were acquired using a Bruker D8-Focus Bragg-Brentano X-ray powder diffractometer equipped with a Cu K $\alpha$  ( $\lambda$  = 1.5418Å) source and operated at an accelerating voltage of 40 kV. Low-temperature powder XRD patterns were acquired using a Bruker-AXS Venture X-ray (kappa geometry) diffractometer with Cu-I $\mu$ s X-ray tube (K $\alpha$  = 1.5418 Å) with an Oxford Cyrosystem Low Temperature Attachment (RT – 110 K). Measurements were acquired at -163°C.

**XANES Spectroscopy.** B K-edge XANES spectra were acquired in the energy range of 185—210 eV at the Variable Line Spacing-Plane Grating Monochromator (VLS-PGM) beamline (E/ $\Delta$ E > 10,000) of the Canadian Light Source at the University of Saskatchewan in Saskatoon, SK. The samples were mounted in a UHV chamber a pressure of 1×10<sup>-8</sup> Torr. The XANES spectra were measured using the high-energy grating of the beamline yielding a spectral resolution of ca. 0.1 eV with entrance and exit slit widths of 100  $\mu$ m. A microchannel plate detector was used to collect the fluorescence yield (FLY) signal. All spectra recorded were normalized to the intensity of the photon beam as measured by the drain current of a Ni mesh (transmission 90%) situated upstream of the sample.

Three B-doped VO<sub>2</sub> samples were analyzed: relaxed-monoclinic (M<sub>1</sub>)  $B_{0.052}VO_2$ , unrelaxed-M<sub>1</sub>  $B_{0.004}VO_2$ , and rutile (R)  $B_{0.052}VO_2$ . The relaxed-M<sub>1</sub>  $B_{0.05}VO_2$  sample was relaxed to room temperature in the DSC using the thermal profile given in **Figure S11**. To assess the extent of thermal-relaxation, DSC scans of a small aliquot of the relaxed-M<sub>1</sub>  $B_{0.052}VO_2$  sample (shown in **Figure S12**) was run in parallel to the XANES measurements. The R  $B_{0.052}VO_2$  sample was an additional  $B_{0.052}VO_2$  sample that was reset immediately prior to the XANES measurement by heating to  $100^{\circ}$ C (ensuring that the sample was not in the relaxed-M<sub>1</sub> state), and cooling to room

temperature. XANES analysis of unrelaxed B-doped VO<sub>2</sub> was done using  $B_{0.004}VO_2$  because the MIT temperature of unrelaxed- $M_1$   $B_{0.052}VO_2$  sample is well below the room temperature measurement making the structure in the R phase. The MIT for  $B_{0.004}VO_2$  is  $58^{\circ}C$ . The  $B_{0.004}VO_2$  sample was reset immediately prior to the XANES measurement by heating to  $100^{\circ}C$  (ensuring that the sample was not in the relaxed- $M_1$  state), and cooling to room temperature.

**Scanning Electron Microscopy.** SEM images of the nanowires were collected on a Tescan MIRA3 FE-SEM (**Figure S1A**) and a Tescan FERA3 FIB-SEM (**Figure S1B**) operated at an accelerating voltage of 20 kV for both instruments.

**First-Principles DFT Calculations.** Prior to first-principles calculations, interstitial sites in the monoclinic ( $P2_1/c$ ) and tetragonal ( $P_4/2_{mnm}$ ) phases were located using the cages function implemented in the AFLOW software.<sup>36</sup> The topological search algorithm selects for unique sites within a unit cell by analyzing the site symmetries within the respective space group. Boron-doped structures were generated from the list of irreducible sites and subsequently relaxed according to the specified DFT parameters.

The atomistic, electronic structures and total energies were calculated using first-principles DFT,<sup>51,52</sup> as implemented in the Vienna ab-initio simulation package (VASP). The projector augmented wave (PAW)<sup>53</sup> method was used to describe the electronic configurations of the relevant elements and the exchange-correlation energy functional was modeled using the GGA with the Perdew-Burke-Ernzerhof (PBE) form.<sup>54</sup> A plane wave basis set with an energy cutoff of 533 eV was employed. Considering the strongly correlated d electrons for vanadium, a Hubbard parameter U is applied to the PBE functional in the approach proposed by Dudarev et al. 55, with  $U_{\rm eff} = 3.4$  eV. As illustrated in Figure S10, this value of U captures the insulating nature of the monoclinic polymorph and the metallic nature of the tetragonal polymorph. The doped 97-atom supercells were generated by replicating the monoclinic and rutile unit cells by 2×2×2 and 2×2×4, respectively. The pristine V<sub>32</sub>O<sub>64</sub> supercells were fully relaxed. For the boron doped structures generated from the supercells, all the V, O, and B atoms were subsequently relaxed. Potential diffusion pathways and the corresponding energy barriers for B atom within M<sub>1</sub> VO<sub>2</sub> were examined using the nudged elastic band (NEB) method, 45,46 where a total of three images were interpolated and subsequently relaxed between the initial and final configurations. The convergence tolerance for electronic relaxation was set to  $10^{-7}$  eV, and the maximum residual force for ionic relaxation was set to  $<0.01 \text{ eV Å}^{-1}$ . A Monkhorst-Pack mesh with at least 5000 k-points per reciprocal atom was used for the Brillouin zone integration.

**DFT Calculations of the Formation Energies of Charged Defects.** To mimic the dilute limit, the unit cell structure is enlarged to  $2\times2\times2$  supercell, and due to the high computational cost the k-point sampling is reduced to  $2\times2\times2$  accordingly. Spin polarization is included for all the defect calculations. The defect formation energy is defined by  $\Delta E^f(D,q) = E(D,q) - E(\text{bulk}) - \Sigma n_i \mu_i + q(\epsilon_F + \epsilon_{VBM}) + E_{corr}$ , where E(D,q) and E(bulk) refer to the total energy of the pristine

host cell and the supercell with defect D in charge state q, respectively.  $\mu_i$  is the chemical potential of species i involved in the defect, and  $n_i$  is the number of the atoms added ( $n_i > 0$ ) or removed ( $n_i < 1$ ). In this work, we consider three types of defects: B-on-V substitutional defect, B-on-O substitutional defect, and B interstitial defect.  $q\epsilon_F$  represents the electron reservoir, and  $\epsilon_F$  is the Fermi level with respect to the valence band maximum  $\epsilon_{VBM}$  in the perfect cell. The range of the chemical potential for each species is determined by the stability of VO<sub>2</sub> relative to the elemental phases and other competing compounds. The last term  $E_{corr}$  in the above equation is the correction to the formation energy caused by the interaction between the defect charge and its images and the potential alignment between the defect and host cells under the periodic boundary condition employed in the DFT calculations.<sup>57</sup> To determine the equilibrium Fermi level, we conduct native defect calculations assuming the point defects play a dominating role and solve self-consistent equations under charge neutrality condition. More details are provided in the supporting information.

XANES Simulation Calculations. The simulation of X-ray absorption spectra and the orbital density plot was done using the PWscf code in the Quantum ESPRESSO package. The sampling of the Brillouin zone was achieved using the Shirley optimal basis set.<sup>58,59</sup> A constant value of 192.0 eV is added to all the theoretical spectra in order to align with the experimental spectra. For the simulation of the B K-edge XANES spectra, a uniform k-point sampling grid of 2 × 2 × 2 was used. The B K-edge simulation uses the eXcited Core Hole X-ray Absorption Spectra (XCH-XAS) approach, in which an electron is removed from the 1s inner shell of the excited B-atom within the VO<sub>2</sub> unit cell to account for the excited state core-hole interactions.<sup>43,44</sup> The inclusion of the core—hole perturbation is not explicit but is instead accounted for using a modified boron pseudopotential with one less electron in the 1s orbital for the B K-edge. The excited electron is included in the occupied electronic structure, and the entire electronic system is relaxed to its ground state within DFT. In order to reproduce the instrumental broadening observed in experimental spectra, a broadening of 0.2 eV was used for the simulated spectra.

In Situ DSC and Water Bath Relaxation Experiments. In situ DSC annealing experiments were conducted using the instrument define above. For all experiments described in Figure 3A, the sample was scanned at 10°C/min from -60°C to 100°C at least once before continuing along a given temperature outlined in the bottom section of Figure 3A. This protocol ensured that the sample was fully "reset" into the unrelaxed state before annealing.

Water bath relaxation experiments were preformed using a PolyScience (AP07R) circulating bath with a working temperature range of -40°C—200°C. Samples were sealed in a water-tight glass vial in an inert Ar environment. Immediately prior to the experiment, the samples were heated to 100°C for 20 minutes to convert to the R phase before being rapidly cooled to -78°C with dry ice.

## **Acknowledgements**

EJB acknowledges support from the Data-Enabled Discovery and Design of Energy Materials (D³EM) program funded by the National Science Foundation under DGE-1545403. RA and RV also acknowledge the support from the Air Force Office of Scientific Research under AFOSR-FA9550-78816-1-0180 (Program Manager: Dr. Ali Sayir). EB, AP, T.E.G.A., L.D.J., and SB acknowledge support from the NSF under DMR 180966. XQ acknowledges support from NSF under DMR-1753054. The authors wish to thank N. Bhuvanesh of the TAMU Department of Chemistry X-Ray Diffraction Laboratory for his help with the low-temperature XRD experiments. Part of the research described in this paper was performed at the Canadian Light Source, which is supported by the Natural Sciences and Engineering Research Council of Canada, the National Research Council Canada, the Canadian Institutes of Health Research, the Province of Saskatchewan, Western Economic Diversification Canada, and the University of Saskatchewan. DFT calculations were carried out at the Texas Advanced Computing Center (TACC) at the University of Texas at Austin and at the Texas A&M High Performance Research Computing.

## **Author Contributions**

This work is the result of a continued collaboration between research groups directed by SB, PS, RA, and XQ. DGS and EJB conducted the experimental work, analyzed the data, wrote the manuscript, and contributed equally to this work. RV and BZ performed the DFT calculations. AP preformed the XANES simulations. TDB conducted the symmetry analysis. DGS and TEGA synthesized the B-doped VO<sub>2</sub>. HC preformed the SEM measurements. LRD performed the XANES measurements under the supervision of LZ.

## **Competing Interests Statement**

The authors declare no competing interests.

## References

- 1. Kumar, S., Strachan, J. P. & Williams, R. S. Chaotic dynamics in nanoscale NbO<sub>2</sub> Mott memristors for analogue computing. *Nature* **548**, 318 (2017).
- 2. Shi, J., Ha, S. D., Zhou, Y., Schoofs, F. & Ramanathan, S. A correlated nickelate synaptic transistor. *Nat. Commun.* **4**, 2676 (2013).
- 3. Marley, P. M., Horrocks, G. a, Pelcher, K. E. & Banerjee, S. Transformers: The Changing Phases of Low-Dimensional Vanadium Oxide Bronzes. *Chem. Commun.* **51**, 5181–5198 (2015).
- 4. Bibes, M. & Barthélémy, A. Towards a magnetoelectric memory. *Nat. Mater.* 7, 425 (2008).
- 5. Hannink, R. H. J., Kelly, P. M. & Muddle, B. C. Transformation Toughening in Zirconia-Containing Ceramics. *J. Am. Ceram. Soc.* **83**, 461–487 (2000).
- 6. Hudak, B. M. *et al.* Real-time atomistic observation of structural phase transformations in individual hafnia nanorods. *Nat. Commun.* **8**, 15316 (2017).
- 7. James, R. D. & Hane, K. F. Martensitic transformations and shape-memory materials. *Acta*

- Mater. 48, 197–222 (2000).
- 8. Song, Y., Chen, X., Dabade, V., Shield, T. W. & James, R. D. Enhanced reversibility and unusual microstructure of a phase-transforming material. *Nature* **502**, 85–88 (2013).
- 9. Andrews, J. L., Santos, D. A., Meyyappan, M., Williams, R. S. & Banerjee, S. Review Building Brain-Inspired Logic Circuits from Dynamically Switchable Transition-Metal Oxides. *Trends Chem.* **1**, 711–726 (2019).
- 10. Braham, E. J. *et al.* Modulating the Hysteresis of an Electronic Transition: Launching Alternative Transformation Pathways in the Metal-Insulator Transition of Vanadium(IV) Oxide. *Chem. Mater.* **30**, 214–224 (2018).
- 11. Brito, W. H., Aguiar, M. C. O., Haule, K. & Kotliar, G. Dynamic electronic correlation effects in NbO<sub>2</sub> as compared to VO<sub>2</sub> *Phys. Rev. B* **96**, 195102 (2017).
- 12. Yuan, X., Zhang, Y., Abtew, T. A., Zhang, P. & Zhang, W. VO<sub>2</sub>: Orbital competition, magnetism, and phase stability. *Phys. Rev. B* **86**, 235103 (2012).
- 13. Whittaker, L., Patridge, C. J. & Banerjee, S. Microscopic and nanoscale perspective of the metal-insulator phase transitions of VO<sub>2</sub>: Some new twists to an old tale. *J. Phys. Chem. Lett.* **2**, 745–758 (2011).
- 14. Asayesh-Ardakani, H. *et al.* Atomic Origins of Monoclinic-Tetragonal (Rutile) Phase Transition in Doped VO<sub>2</sub> Nanowires. *Nano Lett.* **15**, 7179–7188 (2015).
- 15. Booth, J. & Casey, P. Anisotropic Structure Deformation in the VO2 Metal-Insulator Transition. *Phys. Rev. Lett.* **103**, 86402 (2009).
- 16. Pouget, J. P. *et al.* Dimerization of a linear Heisenberg chain in the insulating phases of V<sub>1-x</sub>Cr<sub>x</sub>O<sub>2</sub>. *Phys. Rev. B* **10**, 1801–1815 (1974).
- 17. Ghedira, M., Vincent, H., Marezio, M. & Launay, J. C. Structural Aspects of the Metal-Insulator Transitions in V<sub>0.985</sub>Al<sub>0.015</sub>O<sub>2</sub>. *J. Solid State Chem.* **22**, 423–438 (1977).
- 18. Quackenbush, N. F. *et al.* Stability of the M2 phase of vanadium dioxide induced by coherent epitaxial strain. *Phys. Rev. B* **94**, 1–6 (2016).
- 19. Filinchuk, Y. *et al.* In Situ Diffraction Study of Catalytic Hydrogenation of VO<sub>2</sub>: Stable Phases and Origins of Metallicity. *J. Am. Chem. Soc.* **136**, 8100–8109 (2014).
- 20. Braham, E. J., Andrews, J. L., Alivio, T. E. G., Fleer, N. A. & Banerjee, S. Stabilization of a Metastable Tunnel-Structured Orthorhombic Phase of VO<sub>2</sub> upon Iridium Doping. *Phys. status solidi* 1700884 (2018).
- 21. Zhang, J. J., He, H. Y., Xie, Y. & Pan, B. C. Boron-Tuning Transition Temperature of Vanadium Dioxide from Rutile to Monoclinic Phase. *J. Chem. Phys.* **141**, 194707 (2014).
- 22. Alivio, T. E. G. *et al.* A Post-Synthetic Route for Modifying the Metal Insulator Transition of VO<sub>2</sub> by Interstitial Dopant Incorporation. *Chem. Mater.* **29**, 5401–5412 (2017).
- 23. Whittaker, L., Wu, T.-L., Patridge, C. J., Sambandamurthy, G. & Banerjee, S. Distinctive finite size effects on the phase diagram and metal–insulator transitions of tungsten-doped vanadium(iv) oxide. *J. Mater. Chem.* **21**, 5580 (2011).
- 24. Krammer, A. et al. Elevated transition temperature in Ge doped VO<sub>2</sub> thin films. J. Appl.

- Phys. 122, 45304 (2017).
- 25. Fan, W. *et al.* Large kinetic asymmetry in the metal-insulator transition nucleated at localized and extended defects. *Phys. Rev. B Condens. Matter Mater. Phys.* **83**, (2011).
- 26. Wu, J. *et al.* Strain-induced self organization of metal-insulator domains in single-crystalline VO<sub>2</sub> nanobeams. *Nano Lett.* **6**, 2313–2317 (2006).
- 27. Wei, J., Ji, H., Guo, W., Nevidomskyy, A. H. & Natelson, D. Hydrogen stabilization of metallic vanadium dioxide in single-crystal nanobeams. *Nat. Nanotechnol.* **7**, 357–362 (2012).
- 28. Strelcov, E. *et al.* Doping-Based Stabilization of the M2 Phase in Free-Standing VO<sub>2</sub> Nanostructures at Room Temperature. *Nano Lett.* **12**, 6198–6205 (2012).
- 29. Zhang, S., Chou, J. Y. & Lauhon, L. J. Direct Correlation of Structural Domain Formation with the Metal Insulator Transition in a VO<sub>2</sub> Nanobeam. *Nano Lett.* **9**, 4527–4532 (2009).
- 30. Kachi, S., Kosuge, K. & Okinaka, H. Metal-insulator transition in V<sub>n</sub>O2<sub>n-1</sub>. *J. Solid State Chem.* **6**, 258–270 (1973).
- 31. Budai, J. D. *et al.* Metallization of vanadium dioxide driven by large phonon entropy. *Nature* **515**, 535–539 (2014).
- 32. Clarke, H. *et al.* Nucleation-controlled hysteresis in unstrained hydrothermal VO<sub>2</sub>. *Phys. Rev. Mater.* **2**, 103402 (2018).
- 33. Pauling, L. Atomic Radii and Interatomic Distances in Metals. *J. Am. Chem. Soc.* **69**, 542–553 (1947).
- 34. Eyert, V. VO2: A novel view from band theory. Phys. Rev. Lett. 107, 2–5 (2011).
- 35. Mukherjee, S. *et al.* Tuning a strain-induced orbital selective Mott transition in epitaxial VO2. *Phys. Rev. B* **93**, 1–5 (2016).
- 36. Curtarolo, S. et al. AFLOW: An Automatic Framework for High-Throughput Materials Discovery. Computational Materials Science 58, (2013).
- 37. Chen, J. G. NEXAFS investigations of transition metal oxides, nitrides, carbides, sulfides and other interstitial compounds. *Surf. Sci. Rep.* **30**, 1–152 (1997).
- 38. Hemraj-Benny, T. *et al.* Investigating the Structure of Boron Nitride Nanotubes by Near-Edge X-Ray Absorption Fine Structure (NEXAFS) Spectroscopy. *Phys. Chem. Chem. Phys.* 7, 1103–1106 (2005).
- 39. Fleet, M. E. & Liu, X. Boron K-Edge XANES of Boron Oxides: Tetrahedral B-O Distances and Near-Surface Alteration. *Phys. Chem. Miner.* **28**, 421–427 (2001).
- 40. Li, D., Bancroft, G. M. & Fleet, M. E. B K-edge XANES of crystalline and amorphous inorganic materials. *J. Electron Spectros. Relat. Phenomena* **79**, 71–73 (1996).
- 41. Fleet, M. E. & Muthupari, S. Coordination of boron in alkali borosilicate glasses using XANES. *J. Non. Cryst. Solids* **255**, 233–241 (1999).
- 42. Lee, S. K. *et al.* Probing of bonding changes in B<sub>2</sub>O<sub>3</sub> glasses at high pressure with inelastic X-ray scattering. *Nat. Mater.* **4**, 851 (2005).
- 43. Prendergast, D. & Galli, G. X-Ray Absorption Spectra of Water from First Principles Calculations. *Phys. Rev. Lett.* **96**, 215502 (2006).

- 44. Parija, A. *et al.* Mapping Catalytically Relevant Edge Electronic States of MoS<sub>2</sub>. *ACS Cent. Sci.* **4**, 493–503 (2018).
- 45. Meng, Y. & Arroyo-de Dompablo, M. First principles computational materials design for energy storage materials in lithium ion batteries. *Energy Environ. Sci.* **2**, 589-609 (2009).
- 46. Rong, Z. *et al.* Materials Design Rules for Multivalent Ion Mobility in Intercalation Structures. *Chem. Mater.* **27**, 6016–6021 (2015).
- 47. Miura, S., Maeda, S. & Nakanishi, N. Pseudoelasticity in Au-Cu-Zn thermoelastic martensite. *Philos. Mag. A J. Theor. Exp. Appl. Phys.* **30**, 565–581 (1974).
- 48. Burkart, M. W. & Read, T. A. Diffusionless phase change in indium-thallium system. *J. Met.* **5**, 1516–1524 (1953).
- 49. S. Basinski, Z. & Christian, J. W. Crystallography of deformation by twin boundary movements in indium-thallium alloys. *Acta Metall.* **2**, 101–116 (1954).
- 50. Otsuka, K. & Ren, X. Mechanism of martensite aging effect. Scr. Mater. 50, 207–212 (2004).
- 51. Hohenberg, P. & Kohn, W. Inhomogeneous Electron Gas. *Phys. Rev.* **136**, B864–B871 (1964).
- 52. Kohn, W. & Sham, L. J. Self-Consistent Equations Including Exchange and Correlation Effects. *Physical Review* **140**, A1133–A1138 (1965).
- 53. Kresse, G. & Joubert, D. From ultrasoft pseudopotentials to the projector augmented-wave method. *Phys. Rev. B* **59**, 1758–1775 (1999).
- 54. Burke, K., Perdew, J. P. & Wang, Y. Derivation of a Generalized Gradient Approximation: The PW91 Density Functional. *Electronic Density Functional Theory: Recent Progress and New Directions.* in (eds. Dobson, J. F., Vignale, G. & Das, M. P.) 81–111 (Springer US, 1998).
- 55. Dudarev, S. & Botton, G. Electron-energy-loss spectra and the structural stability of nickel oxide: An LSDA+U study. *Phys. Rev. B Condens. Matter Mater. Phys.* **57**, 1505–1509 (1998).
- 56. Freysoldt, C. *et al.* First-principles calculations for point defects in solids. *Rev. Mod. Phys.* **86**, 253–305 (2014).
- 57. Kumagai, Y. & Oba, F. Electrostatics-based finite-size corrections for first-principles point defect calculations. *Phys. Rev. B Condens. Matter Mater. Phys.* **89**, (2014).
- 58. Prendergast, D. & Louie, S. G. Bloch-state-based interpolation: An efficient generalization of the Shirley approach to interpolating electronic structure. *Phys. Rev. B* **80**, 235126 (2009).
- 59. Shirley, E. L. Optimal basis sets for detailed Brillouin-zone integrations. *Phys. Rev. B* **54**, 16464–16469 (1996).